Monthly Notices
of the
ROYAL ASTRONOMICAL SOCIETY

MNRAS **478,** 2835–2849 (2018)
Advance Access publication 2018 May 18

doi:10.1093/mnras/sty1304

An all-sky survey of circular polarization at 200 MHz

Emil Lenc,[1,2,3]★ Tara Murphy,[1,2] C. R. Lynch,[1,2] D. L. Kaplan[4] and S. N. Zhang[5]

[1]*Sydney Institute for Astronomy, School of Physics, The University of Sydney, NSW 2006, Australia*
[2]*ARC Centre of Excellence for All-sky Astrophysics (CAASTRO), The University of Sydney, NSW 2006, Australia*
[3]*CSIRO Astronomy and Space Science, PO Box 76, Epping, NSW 1710, Australia*
[4]*Department of Physics, University of Wisconsin–Milwaukee, Milwaukee, WI 53201, USA*
[5]*School of Astronomy and Space Science, Nanjing University, 163 Xianlin Avenue, Nanjing 210023, China*

Accepted 2018 May 12. Received 2018 April 26; in original form 2018 February 28

ABSTRACT

We present results from the first all-sky radio survey in circular polarization. The survey uses the Murchison Widefield Array (MWA) to cover 30 900 sq deg, over declinations south of +30° and north of −86° centred at 200 MHz (over a 169–231 MHz band). We achieve a spatial resolution of ∼3 arcmin and a typical sensitivity of 3.0 mJy PSF^{-1} over most of the survey region. We demonstrate a new leakage mitigation technique that reduces the leakage from total intensity into circular polarization by an order of magnitude. In a blind survey of the imaged region, we detect 14 pulsars in circular polarization above a 6σ threshold. We also detect six transient sources associated with artificial satellites. A targeted survey of 2376 pulsars within the surveyed region yielded 33 detections above 4σ. Looking specifically at pulsars previously detected at 200 MHz in total intensity, this represents a 35 per cent detection rate. We also conducted a targeted survey of 2400 known flare stars, this resulted in two tentative detections above 4σ. A similar targeted search for 1506 known exoplanets in the field yielded no detections above 4σ. The success of the survey suggests that similar surveys at longer wavelength bands and of deeper fields are warranted.

Key words: radio continuum: planetary systems – (stars:) pulsars: general – plasmas.

1 INTRODUCTION

The vast majority of all-sky radio surveys to date have focused on sources emitting in total intensity (Stokes I) e.g. Westerbork Northern Sky Survey (Rengelink et al. 1997), Sydney University Molonglo Sky Survey (Mauch et al. 2003), Galactic and Extragalactic All-Sky MWA Survey (GLEAM; Hurley-Walker 2017), and the GMRT 150 MHz All-sky Radio Survey First Alternative Data Release (TGSS ADR1; Intema et al. 2017). The exception is the NRAO VLA Sky Survey (Condon et al. 1998), which also considered linear (Stokes Q and Stokes U) polarization (Taylor, Stil & Sunstrum 2009). However, to date, there have been no all-sky radio surveys in circular polarization (Stokes V).

Numerous astrophysical sources are known to emit circular polarization with relatively high degrees of fractional polarization (≥1 per cent). These include pulsars (You & Han 2006; Noutsos et al. 2015; Johnston & Kerr 2017), flare stars (Lynch et al. 2017b), and Jupiter (Seaquist 1969). It is also anticipated that some exoplanets may also emit circular polarization (Winglee, Dulk & Bastian 1986; Zarka et al. 2001; Murphy et al. 2015; Lynch et al. 2017a). Weak levels of circular polarization (0.01–1 per cent) have been observed in active galactic nuclei (AGNs; Komesaroff et al. 1984; Weiler & de Pater 1983; Rayner, Norris & Sault 2000; Aller & Aller 2012), intra-day variable sources (Macquart et al. 2000), and are also expected in diffuse Galactic synchrotron emission (Enßlin et al. 2017) at fractions of less than 0.1 per cent.

Observations of circular polarization can inform us about the physical processes within these sources and propagation effects along the line of sight. Coherent emission processes can generate highly circularly polarized emission (Macquart 2002, 2003), whereas circular polarization resulting from synchrotron radiation is generally very weak. Propagation effects can also cause circular polarization through scintillation in a magnetized plasma, refraction effects near black holes, and linearly polarized radiation passing through a relativistic plasma (Macquart 2002, 2003). To confirm the source of circularly polarized emission generally requires a combination of detailed observations and theoretical modelling (e.g. O'Sullivan et al. 2013).

Compared to total intensity, only a small fraction of sources emit circularly polarized radiation resulting in a lower classical confusion limit. As such, for instruments that are confusion limited in total intensity, such as the Murchison Widefield Array (MWA; Tingay et al. 2013a), greater sensitivity can be achieved when observing in circular polarization. This is particularly beneficial for sources that have high degrees of fractional circular polarization; however, the

★ E-mail: Emil.Lenc@csiro.au.; Tara.Murphy@sydney.edu.au

gain in sensitivity diminishes for sources that exhibit low degrees of fractional circular polarization. A positive aspect of this is that most sources are generally weak in circular polarization and so do not greatly contribute to side-lobe confusion. Therefore deconvolution is unnecessary, greatly simplifying processing.

Continuum observations in circular polarization may also aid in the detection of pulsars missed using conventional means. For example, pulsars with complex orbits, sub-millisecond pulsars, and pulsars exhibit significant pulse broadening (Bhat et al. 2004; Geyer et al. 2017; Xue et al. 2017). Traditional search methods assume regular, well-separated pulses, but accelerations in compact orbits lead to significant computational difficulties and broadening can cause individual pulses to blend. Despite this, if the pulsar is sufficiently steep-spectrum, low-frequency imaging searches (e.g. Frail et al. 2018) may discover a number of pulsars that would be otherwise missed. Even this can be problematic, though, as the noise in total intensity images can be significantly higher in the Galactic plane where most pulsars are found. Therefore searches done in circular polarization may allow the deepest searches for continuum emission independent of other pulsar properties. Searching in circular polarization is further beneficial compared to searches in Stokes I continuum as very few sources exhibit circularly polarized emission and so the number of candidate sources greatly reduces. Transient searches are also simplified as they are less affected by source confusion (e.g. Lynch et al. 2017b).

Despite the potential for discovery available with observations in circular polarization, there have been no all-sky surveys to date. All observations have been targeted towards specific known source populations, e.g. AGN (Rayner et al. 2000; Cenacchi et al. 2011), pulsars (Johnston & Kerr 2017), and exoplanets (Murphy et al. 2015). For the most part, all-sky observations of circular polarization have been hindered by instrumental leakage. In the case of dipole-based instruments, such as the MWA, this leakage is primarily caused by poor models of the primary beam (Sutinjo et al. 2015). For the MWA, the effect is particularly pronounced at higher frequencies and towards the edge of the beam. Lenc et al. (2017) demonstrated that polarization leakage observed with the MWA could be mitigated in drift-scan observations by modelling the leakage pattern across the beam and then subtracting it.

In this paper, we present the first all-sky radio survey in circular polarization. The survey covers the entire Southern sky ranging in declination from -85° to $+30^\circ$ at a frequency of 200 MHz. We use data originally observed as part of the GLEAM survey (Wayth et al. 2015; Hurley-Walker et al. 2017). In the process of performing this survey, we also tested the effectiveness of leakage mitigation. Throughout this paper, we have adopted the PSR/IEEE convention for left-handed and right-handed circular polarizations (van Straten et al. 2010) that are of positive and negative signs, respectively.

2 OBSERVATIONS AND DATA ANALYSIS

2.1 Observations

We used archival visibility data observed as part of GLEAM (Wayth et al. 2015; Hurley-Walker et al. 2017). The observations used a drift-scan observing mode where tiles always point at the meridian. As such, instrumental systematics are minimized by maintaining a consistent observing set-up. To allow direct comparison to the GLEAM deep wide-band survey data (Hurley-Walker et al. 2017), we used the 169–200 MHz and 200–231 MHz frequency bands. Inaccuracies in the MWA beam model make these two frequency bands more prone to polarization leakage than the three lower bands (Sutinjo et al. 2015; Lenc et al. 2016; Sokolowski et al. 2017), so this data set is well-suited to testing the effectiveness of our polarization leakage subtraction technique. A list of the individual GLEAM drift-scan observations used is summarized in Table 1.

Table 1. GLEAM first-year observing parameters. $N_{\rm flag}$ is the number of MWA tiles (of the 128 available) that are flagged. The calibrator is used to determine initial bandpass, phase, and flux density scale corrections.

Date	Dec.	RA range (h)	$N_{\rm flag}$	Calibrator
2013-08-08	+1.6°	19.5–3.5	3	3C 444
2013-08-09	−55.0°	19.5–3.5	11	3C 444
2013-08-10	−26.7°	19.5–3.5	11	3C 444
2013-08-17	+18.6°	19.5–3.5	4	3C 444
2013-08-18	−72.0°	19.5–3.5	6	3C 444[a]
2013-08-22	−13.0°	19.5–3.5	1	3C 444
2013-08-25	−40.0°	19.5–3.5	1	3C 444
2013-11-05	−13.0°	0–8	5	Hydra A
2013-11-06	−40.0°	0–8	6	Hydra A
2013-11-07	+1.6°	0–8	4	Hydra A
2013-11-08	−55.0°	0–8	6	Hydra A
2013-11-11	+18.6°	0–8	8	Hydra A
2013-11-12	−72.0°	0–8	18	Hydra A
2013-11-25	−26.7°	0–8	0	Hydra A
2014-03-03	−26.7°	6–16	0	Hydra A
2014-03-04	−13.0°	6–16	0	Hydra A
2014-03-06	+1.6°	6–16	1	Hydra A
2014-03-08	+18.6°	6–16	1	Hydra A
2014-03-09	−72.0°	6–16	1	Hydra A
2014-03-16	−40.0°	6–16	1	Hydra A
2014-03-17	−55.0°	6–16	1	Hydra A
2014-06-09	−26.7°	12–22	3	3C 444
2014-06-10	−40.0°	12–22	4	3C 444
2014-06-11	+1.6°	12–22	5	3C 444
2014-06-12	−55.0°	12–18.5	6	Hercules A
2014-06-13	−13.0°	12–19	5	Hercules A
2014-06-14	−72.0°	12–22	4	3C 444
2014-06-15	+18.6°	12–22	5	3C 444
2014-06-16[b]	−13.0°	18.5–22	3	3C 444
2014-06-18[c]	−55.0°	15–22	0	3C 444

Notes. [a]Calibration from previous day (2013 August 17) re-used.
[b]Partial reobservation of 2014 June 13 drift scan.
[c]Partial reobservation of 2014 June 12 drift scan.

2.2 Data reduction

We calibrated the data using the real-time calibration and imaging system, referred to as the RTS (Mitchell et al. 2008; Ord et al. 2010), using the procedure outlined in Lenc et al. (2016) for point source polarimetry. Calibration was performed per epoch using a calibrator observation for that specific epoch (see Table 1), apart from the 2013 August 18 epoch where the calibration solution for that day was poor and so a solution from the previous day was used.

Archival online flagging (Offringa, van de Gronde & Roerdink 2012) was applied to reduce the effects of radio frequency interference. To minimize sidelobe confusion and reduce sensitivity to large-scale structure, robust weighting was used with a robustness of -1 and only baselines longer than 50λ were utilized. Dirty image cubes were created for each 2-min snapshot using the RTS at full 40 kHz spectral resolution and over a $25^\circ \times 25^\circ$ region centred on the beam pointing location. All images were $2\,187 \times 2\,187$ pixels in extent and with a pixel size of ∼41 arcsec, this equates to a sampling of ∼5 pixels across the beam at 200 MHz. The spectral cubes were

averaged in frequency to create 2-min snapshot images for Stokes I, Q, U, and V.

2.3 Beam modelling and leakage

The true beam pattern of the MWA, as measured empirically by imaging field sources, differs significantly from the analytic beam pattern at the higher end of the MWA band and/or when observing at lower elevation (Sutinjo et al. 2015). This discrepancy results in position-dependent flux density scaling effects in Stokes I (Hurley-Walker et al. 2014, 2017) and polarization leakage in Stokes Q, U, and V (Sutinjo et al. 2015). The most significant source of leakage is from Stokes I as this is where the sky signal dominates. In general, Stokes Q exhibits the strongest level of leakage but Stokes U and V can be contaminated with as much as ∼5 per cent leakage (Lenc et al. 2017) from Stokes I. For circular polarization, such levels of leakage can result in false detections unless they are corrected for.

For a given epoch and frequency, the leakage pattern for a drift-scan beam will remain fixed for each of the Stokes parameters. The nature of the leakage pattern is a function of the calibrator location within the calibrator beam pointing, the beam pointing used for the calibrator scan, and the beam pointing used for the drift scan. To overcome the limitations and errors associated with the analytic beam model, we measured the effect of the beam on known GLEAM sources as they drift through the beam. It is important to note that deconvolution is not performed on the snapshot images. This ensured that the PSF (point-spread function) characteristics of the leaked component remains consistent between each of the Stokes parameters for a given snapshot. A secondary benefit is that the processing was greatly simplified, enabling real-time processing. As weaker GLEAM sources are more likely to be dominated by sidelobe confusion, we excluded them from the sampling process. For this reason, we only consider GLEAM field sources that have a peak flux density in Stokes I greater than 3 Jy PSF^{-1}. For each snapshot image, we sample Stokes I, Q, U, and V at the pixel location of each GLEAM field source.

To map the position-dependent leakage for the beam, we assumed that all of the field sources are unpolarized. At low frequencies, this is a reasonable assumption (Lenc et al. 2016) and one that we verify later through our detection statistics. So any measured polarization is assumed to result from beam errors. For circular polarization we grid the measured fractional circular polarization (V/I) at each of the sampled pixel locations. For small fields of view, a simple two-dimensional plane is sufficient to model the leakage across the beam, e.g. Lynch et al. (2017b), however for larger fields there is significant warping in the leakage behaviour and the fit errors increase significantly at the beam edges. To better model the leakage, we fit a two-dimensional quadratic surface (over both spatial directions) to the grid in order to interpolate over the entire beam. Examples of this fitting are shown in Fig.1 for drift scans at three different points on the meridian.

The leakage into any given Stokes parameter will be a mix of leakage from each of the other Stokes parameters. As the largest astrophysical signal is in Stokes I, it will dominate the observed leakage into each of the remaining Stokes parameters. So, for each snapshot, the previously fit leakage surface for Stokes V is used as position-dependent scaling factor for the Stokes I map, the scaled Stokes I map is then subtracted from the Stokes V map to remove beam-associated leakage. The same process can also be repeated for Stokes Q and Stokes U but is not described in this paper.

An aspect that is not taken into consideration is solving for XY-phase. Uncorrected XY-phase can result in leakage from Stokes U into Stokes V. Leakage of this form can lead to a false detection in Stokes V for a sufficiently strong linearly polarized source. To solve for XY-phase, at least one strong linearly polarized source would be required in each drift scan. At the time of this survey, such information was unavailable at long wavelengths. However, a survey of linearly polarizd sources is currently being performed with the techniques developed here that will enable such calibration in future (Riseley et. al. 2018). Based on prior observations at 154 MHz, we estimate the leakage from Stokes U to Stokes V to be of order 20–30 per cent (Lenc et al. 2016). However, as linearly polarized sources detected with the MWA are generally weak at long wavelengths, typically <5 per cent linearly polarized (Bernardi et al. 2013; Lenc et al. 2016, 2017; O'Sullivan et al. 2018), 30 per cent leakage would typically result in less than 1.5 per cent of excess signal in Stokes V. Furthermore, for our Stokes V continuum observations, this would only be a potential source of error for sources with particularly low rotation measures ($|\mathrm{RM}| < 3$ rad m^{-2}) as they would otherwise be bandwidth depolarized by >75 per cent over the 61.44 MHz available bandwidth.

2.4 Flux calibration

Errors between the analytic beam model and the true beam can result in position-dependent flux calibration errors. During GLEAM survey processing, this was noted as a declination-dependent effect (Hurley-Walker et al. 2014, 2017), mainly because the mosaicking process dampened the effect in Right Ascension. However, a model of the flux calibration error can be formed using a similar process as that used to model the leakage.

To model and correct for the position-dependent flux calibration errors, rather than measuring leakage, the scaling difference between the known GLEAM flux density for a source and the measured position-dependent flux density is gridded to form a scaling map. This scaling map is then applied to both Stokes I and Stokes V images of each snapshot to correct the flux density of field sources.

2.5 Mosaic creation

Mosaic creation was performed using the software package SWARP (Bertin et al. 2002). A three-stage process was utilized to generate the all-sky mosaics. In the first stage, individual mosaics were formed for each epoch and each observing band. This allowed the quality of the drift scans to be assessed and also avoided limitations of the software associated with the number of individual images that could be mosaicked simultaneously. The second stage combined the individual mosaics for a given frequency band into an all-sky mosaic. Finally, in the third stage, the two bands were combined to form the deep all-sky mosaic.

For the first stage of mosaicking, beam maps were created for each snapshot. During mosaicking, the individual snapshots were weighted against the square of the beam maps to minimize edge effects associated with noise spikes and increased error in the leakage corrections. Mosaics were formed using SWARP with the corrected Stokes I and Stokes V snapshots. Mosaics were also formed using the uncorrected Stokes I and Stokes V snapshots to ultimately allow assessment of the effectiveness of the corrections in the final mosaics. All mosaics were formed with zenith-equal-angle projection and combined weight files were created by SWARP for each of the drift scan mosaics and for each observing band.

For the second stage of mosaicking, we used SWARP to combine the individual drift-scan mosaics in each observing band. The combined weight files generated by SWARP in the first stage were used as image

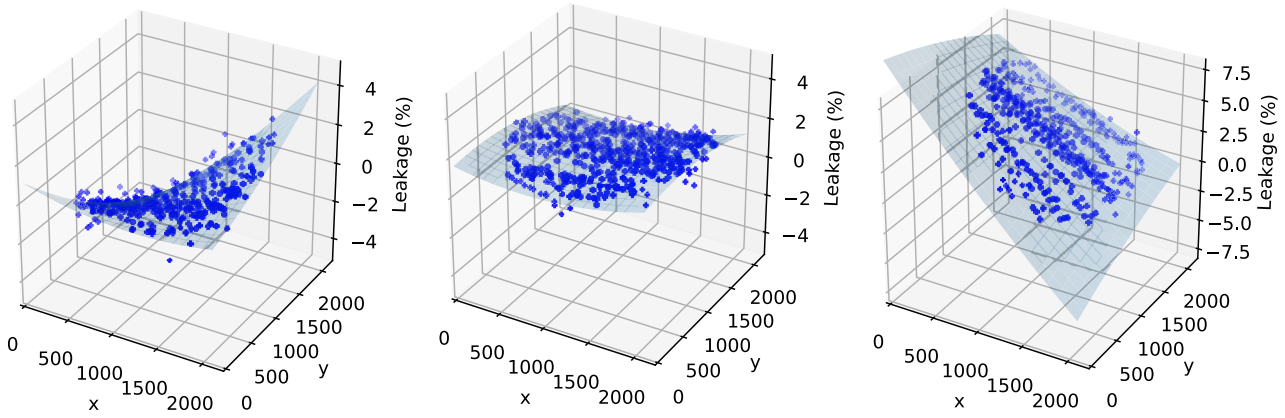

Figure 1. Measured and fitted leakage in Stokes V in the 216 MHz band. The *x*- and *y*- axis are plotted in (*l*, *m*) using units of pixels for a 25° × 25° field (2 187 × 2 187 pixels), where *x* represents the *l* direction and *y* represents the *m* direction. Left: Observations taken from +1.6° drift scan on 2013 August 8. Centre: Observations taken from −26.7° drift scan on 2013 August 10. Right: Observations taken from −72° drift scan on 2013 August 18.

weights during the mosaicking process. The final mosaics for each band were formed with zenithal equal area (ZEA) projection.

In the final stage of mosaicking, the 169–200 MHz and 200–231 MHz mosaics were averaged to form a 200 MHz deep mosaic. This resulted in all-sky maps for the uncorrected Stokes I and Stokes V, and for the corrected Stokes I and Stokes V. Fig. 2 shows a cut-out from the all-sky map showing a Galactic region in the corrected Stokes I and Stokes V maps. Two pulsars, PSRs J0835−4510 and J1157−6224, are clearly detected in the Stokes V map.

2.5.1 *Noise characterization*

The final Stokes V image mosaics contain position-dependent variations in image noise. The main contributing factors to the levels of regional noise are the number of overlapping snapshots in that region, the effectiveness of calibration for the different epochs that contribute to that region (which is a function of the brightness and elevation of the calibrator), and the effectiveness of the leakage subtraction in that region.

At extreme declinations, i.e. +18.6° and −72°, there are no overlapping drift scans to help improve sensitivity and so these field edges have higher noise levels. Some hour angles have higher levels of overlap between drift scans at the same declination and this leads to improved sensitivity in these regions, e.g. between the 0−8 h scans and the 6−16 h scans, there are only 2 h of overlap, whereas between 6−16 h scans and the 12−22 h scans, there are 4 h of overlap.

Regions around bright Stokes I sources can also contribute towards increased Stokes V noise in regions where the leakage modeling is not as effective and in regions where there are extremely bright sources. Even if leakage is reduced to an ambitious level of 0.1 per cent, a 100 Jy source would contribute 100 mJy to Stokes V. Since dirty images are used in processing, PSF sidelobes from these sources would contribute to noise over an extended region around each bright source. Hence we expect increased levels of Stokes V noise around bright sources such as the Crab Nebula and Pictor A.

To map local noise, a 20 × 20 pixel sliding window was used. For each region within the mosaic, the mean and standard deviation are measured, any pixels with a mean subtracted peak exceeding 3σ are excluded, the standard deviation and mean are then measured for the remaining pixels within the sliding window and recorded for that region. The resultant product is a local RMS map as shown in Fig. 3. For the majority of the observable sky below +10° and above −85° the noise levels are typically of order 3 mJy PSF^{-1}. There is a slight excess in noise at around 18 h, this is primarily as a result of the bulk of the Galactic plane passing through this region, however, there is also limit hour-angle coverage in this region and this too will reduce sensitivity in this region.

Fig. 4 shows the proportion of the surveyed region that achieves a given noise level. The overall survey has a median noise level of 3.0 mJy PSF^{-1}. Approximately 25 per cent of the surveyed region achieves a sensitivity better than 2 mJy PSF^{-1} and 75 per cent is better than 5.4 mJy PSF^{-1}. This is a factor of 2–5 improvement compared to the 10 mJy PSF^{-1} sensitivity of GLEAM (Hurley-Walker et al. 2017) in Stokes I with the same weighting scheme.

To verify the Gaussian nature of the noise statistics, we considered all mosaic pixels that sit in regions where the noise was estimated to be within 3.0 ± 0.5 mJy PSF^{-1}. These were fit with a Gaussian with a mean of 0.001 mJy PSF^{-1} and a standard deviation of 3.029 mJy PSF^{-1}. The noise statistics are highly Gaussian with 95.39 per cent of pixels within 2σ, 99.67 per cent within 3σ, 99.986 per cent within 4σ, and 99.9994 per cent within 5σ of the mean. Assuming Gaussian statistics, we would expect ∼78 false detections at the 4σ level, ∼1 at the 5σ level, and ≪1 at the 6σ level over the entire survey area.

2.5.2 *Flux density scale assessment*

To assess the effectiveness of the flux-scale calibration, the flux density of all GLEAM sources with a cataloged peak brightness greater than 3 Jy PSF^{-1} at 200 MHz was measured in the uncorrected and corrected Stokes I mosaics. GLEAM sources in regions where the signal-to-noise was less than 20 were rejected to reduce measurements that are likely to be significantly affected by edge noise or source sidelobes. In total, 1779 GLEAM sources were available for use as suitable probes.

Fig. 5 shows the ratio between the catalogued GLEAM source peak at 200 MHz and the measured Stokes I peak in the 200 MHz mosaic plotted against declination for both the uncorrected and corrected maps. There is a clear declination dependence in the uncorrected data with an overall spread of 22 per cent in the measured flux densities and an absolute scaling of 0.943 compared to those of GLEAM. After correction, the declination dependence is no longer

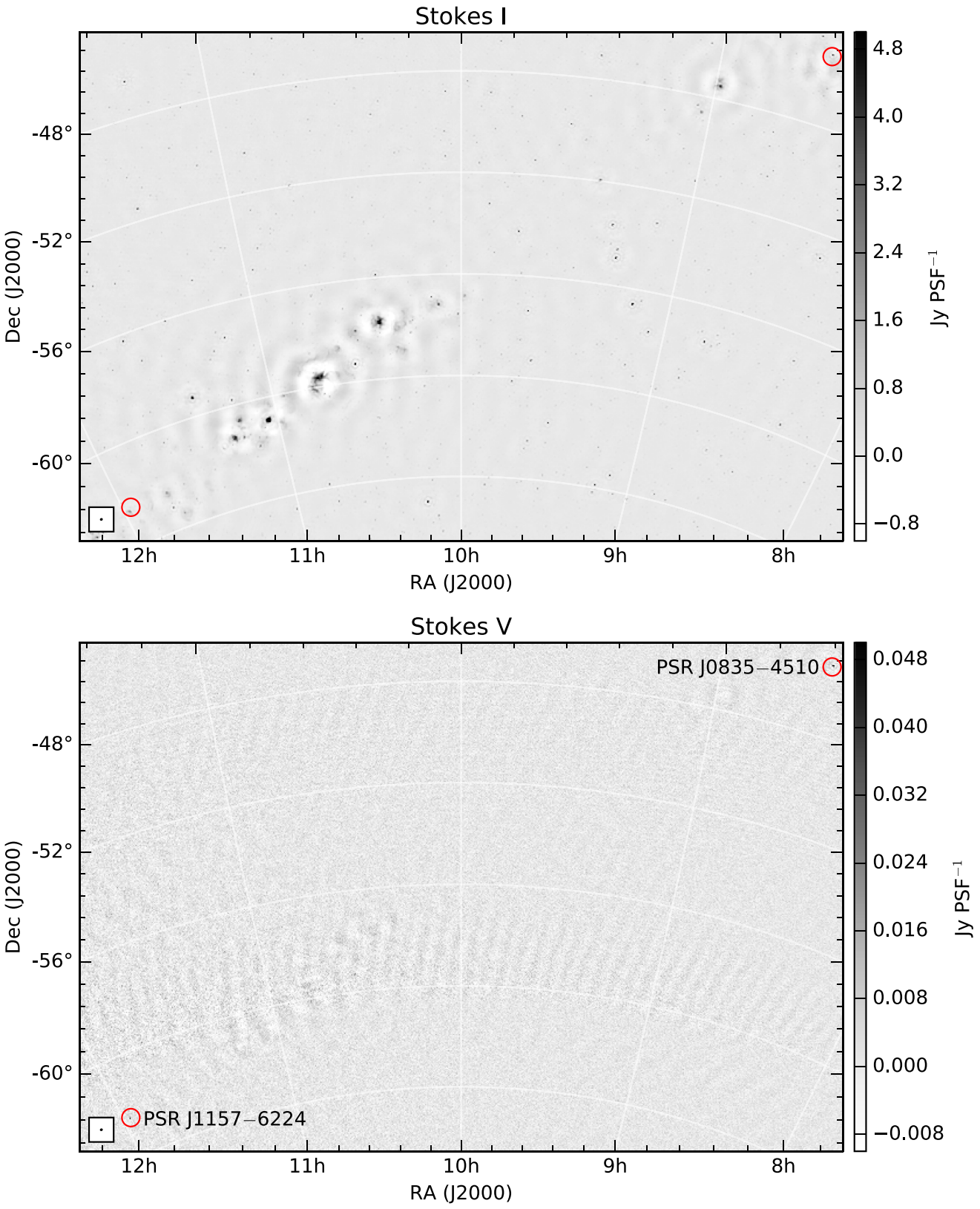

Figure 2. A representative sub-set of the all-sky survey showing a Galactic region in Stokes I and Stokes V at 200 MHz. Two circularly polarized pulsars (circled in red) are detected in this region: PSRs J0835−4510 and J1157−6224. The approximate synthesized beam is shown inset and is ∼3 arcmin in extent. SIN projection was used to generate this map.

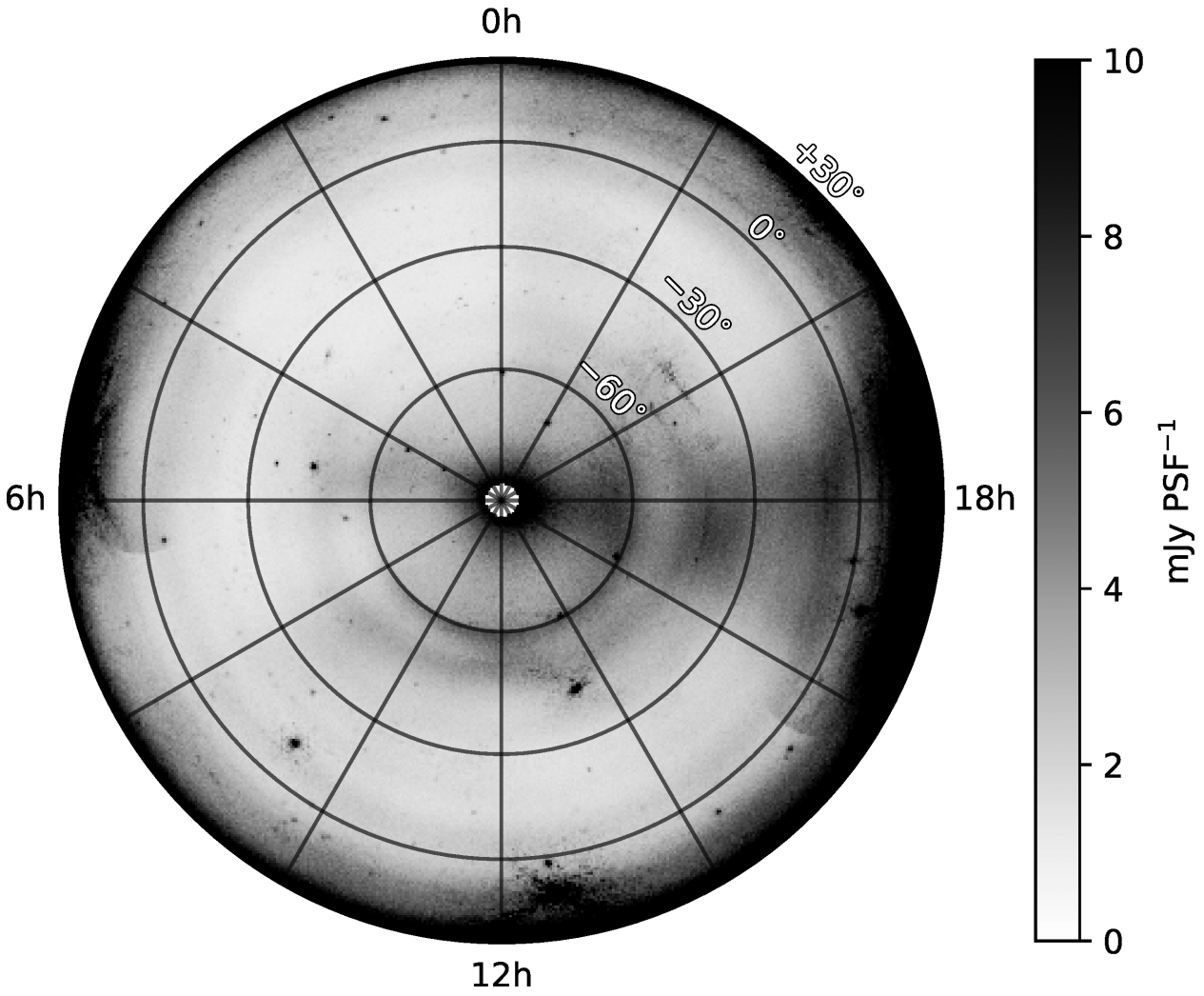

Figure 3. All-sky map of measured RMS image noise in circular polarization in the 200 MHz deep mosaic. A 20 × 20 pixel sliding window was used on the Stokes V mosaic to estimate image noise. ZEA projection is used, centred on a declination of −90°.

prominent with the overall spread reduced to 8.7 per cent and the absolute scaling at 0.984.

Another representation of the flux density scale improvement is shown in Fig. 6. This figure takes the same scaling measurements but maps the results as a function of sky position. The blanked region marks locations where no GLEAM measurements are available. The declination-dependent variations are clearly visible in the uncorrected maps, however, strong RA-dependent variations are also apparent e.g. an abrupt change from overstimating to underestimated the measured flux density at around 12 h at high declinations. This RA-dependent effect results from calibrator source changes and also calibrator beam-former changes from epoch to epoch.

The greatest residual errors in the corrected flux density scale maps appear towards high declinations (particularly at the 18 h and 5 h mark) and towards the Galactic centre. The deviation at high declination is likely due to increased modelling errors at the edge of the map. At the edge of the map there are no further overlapping snapshots to help down-weight the increased fitting errors that are present there during mosaicking. The apparent underestimation of flux density towards the Galactic centre is likely due to sidelobe confusion affecting the sampling of source peak flux densities in that region. If it were a true underestimation of the flux density, then it would affect the entire drift scan rather than just one part of it since the correction is used consistently over the entire drift scan.

2.5.3 *Leakage characterization*

Using a similar approach to that described in Section 2.5.2 for assessing the flux density scale, the 1779 GLEAM sources were also used to probe leakage at various sky locations. For each GLEAM source, the Stokes I and Stokes V flux density was measured at the location of that source.

Fig. 7 shows the percentage of Stokes I to Stokes V leakage as a function of declination before and after correction. Prior to correction the leakage showed a significant declination-dependent behaviour with a typical spread of ∼1 per cent. At certain declinations there were several different bands of leakage. For example, between a declination of −30° and −10° three separate trends are apparent. These different trends, for the same declination, are caused by differences in epoch-to-epoch calibration.

After correction the declination dependence is removed and the typical spread is reduced to 0.12 per cent. Since the drift scans at the highest and lowest declination are edge cases, i.e. they do not

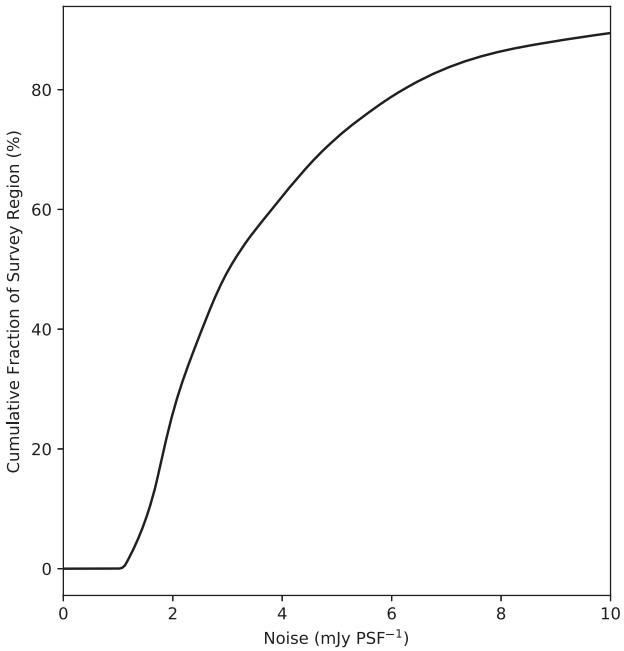

Figure 4. A cumulative histogram showing the fraction of the survey region achieving a given Stokes V image noise limit at 200 MHz. The highest sensitivity achieved is ∼1 mJy PSF^{-1} and ∼10 per cent of the survey region has noise exceeding ∼10 mJy PSF^{-1} (mostly constrained to the edge of the survey region; see Fig. 4.).

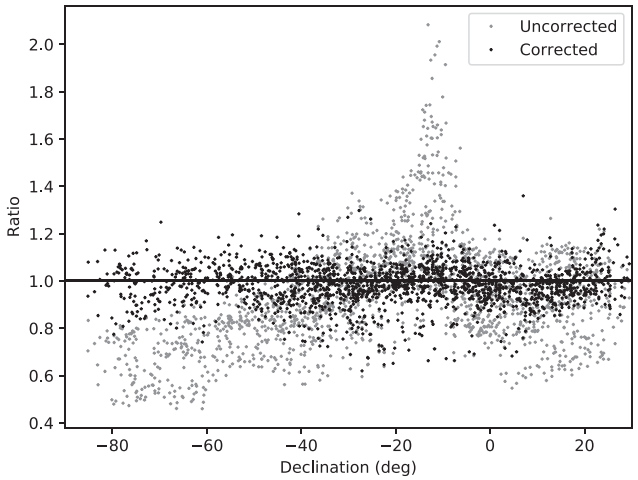

Figure 5. Comparison of survey flux density scale of the 200 MHz deep mosaic with that of the GLEAM survey. Before correction there are declination-dependent effects. There are removed after correction.

have overlapping drift-scans at higher and lower declinations, the model fit to the leakage pattern is not as well constrained. As a result, the spread of leakage increases in these regions. The effect is particularly pronounced above +20° declination where there are limited GLEAM sources to sample against (as a result of decreased sensitivity and regions not sampled by GLEAM).

Mapping the leakage as a function of sky position, as shown in Fig. 8, enables the characteristics of the leakage before and after correction to be analysed more readily. Before correction there are clear bands in declination where the leakage is either highly negative (high declinations) or highly positive (mid and low declinations). The epoch-to-epoch variations noted in Fig. 7, which cause abrupt changes as a function of hour-angle, are seen more clearly, particularly at a declination of ∼−30°.

In the corrected map, the overall leakage is improved by an order of magnitude and no clear trends are apparent for declinations below ∼+20°. Above a declination of ∼+20°, it is apparent that a slight excess of leakage is still present. As described in Section 2.5.2, the model fitting is less constrained in this region and is affected by the reduced number of GLEAM sources that are available within this region. Nonetheless, the leakage is improved by an order of magnitude compared to the uncorrected map.

3 A BLIND SURVEY

A blind search for circularly polarized sources was performed over the entire mosaicked map. The search recorded all pixels in the 200 MHz Stokes V map that were six times greater in flux density than the associated RMS noise in that region based on the local RMS noise map (see Section 2.5.1). Islands of neighbouring detections were grouped as single detections.

In total, 63 unique detections were made above the 6σ level in the 200 MHz Stokes V map. Of these, 41 are associated with bright radio galaxies, 15 with known pulsars, 1 with Jupiter, and 6 with known artificial satellites. The significance of the detection, the fractional circular polarization, and the object type for all 63 sources are plotted in Fig. 9; the figure also includes targeted detections of pulsars, which will be described in Section 4.1. To account for residual leakage that still exists after correcting for Stokes I to Stokes V leakage, a 6σ cut-off is applied to avoid false detections of 'leaked' Stokes I sources. For declinations lower than +20°, this cut-off is set to 0.72 per cent (6σ). For declinations greater than +20°, where there is increased residual leakage, the cut-off is set to 1.8 per cent (6σ) to account for the increased residual leakage in that region. Applying this cut-off, one pulsar (associated with the extremely bright Crab Nebula with a flux density >500 Jy) is rejected and all but three AGNs. All remaining source detections are listed in Table 2.

Table 2 also lists the angular separation between the blind detection and the nearest known radio source. For pulsars, the position is taken from the Australia Telescope National Facility (ATNF) Pulsar Catalog v1.56 (Manchester et al. 2005), AGN positions are taken from the NASA/IPAC Extragalactic Database, and the position of Jupiter is determined for the 2013 November 11 epoch using the PYEPHEM package.[1] Typical astrometric errors of ∼0.3 arcmin are expected based on the PSF size and a signal-to-noise ratio of ∼6. Uncorrected ionospheric effects will have a more dominant effect on astrometric error, contributing an additional error of order ∼1 arcmin at 200 MHz (Loi et al. 2015).

3.1 Pulsars

In total, 14 pulsars were detected in the blind survey. Table 2 lists all of the detected pulsars, the observed characteristics at 200 MHz and observations of circular polarization from literature (where available). Images of two of the detected pulsars, PSRs J1136+1551 and J0835−4510, are shown in Fig.10 and demonstrate that circular polarization of either sign can be observed.

All of the detected pulsars have relatively high fractional circular polarization at 200 MHz (>3 per cent). In our sample, the sign of polarization does not appear to be biased either way with near

[1] http://rhodesmill.org/pyephem

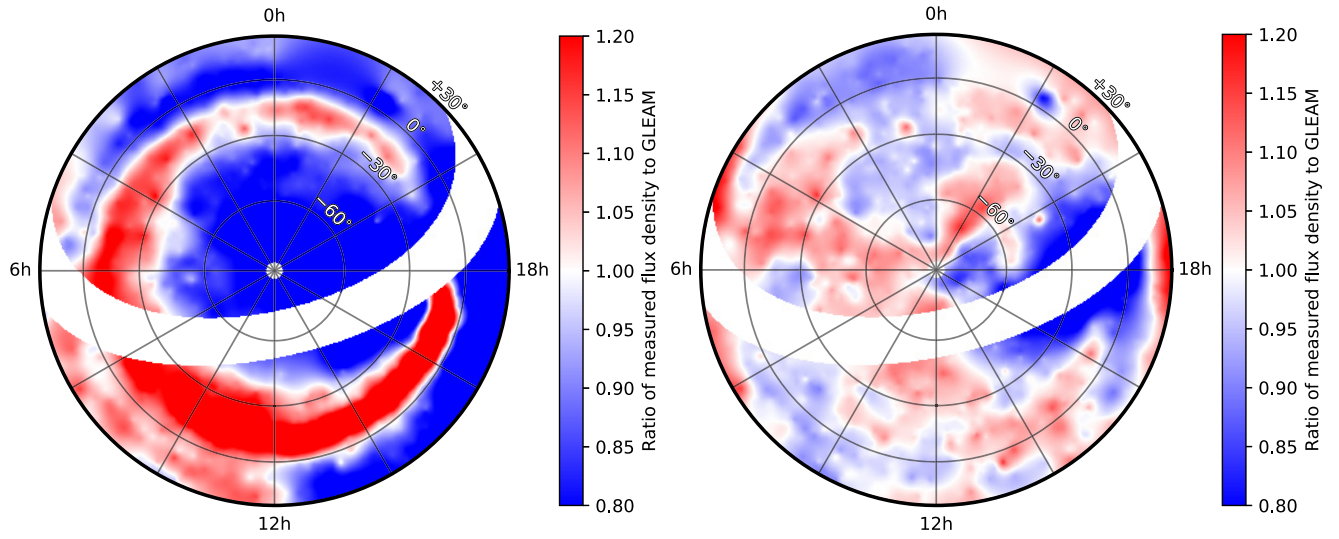

Figure 6. Comparison of survey flux density scale of the 200 MHz deep mosaic with that of the GLEAM survey. The map on the left shows the flux density scale before correction and the map on the right shows the flux density scale after correction. In both maps the blanked strip removes the Galactic plane region as this was not surveyed by GLEAM. ZEA projection is used, centred on a declination of −90°.

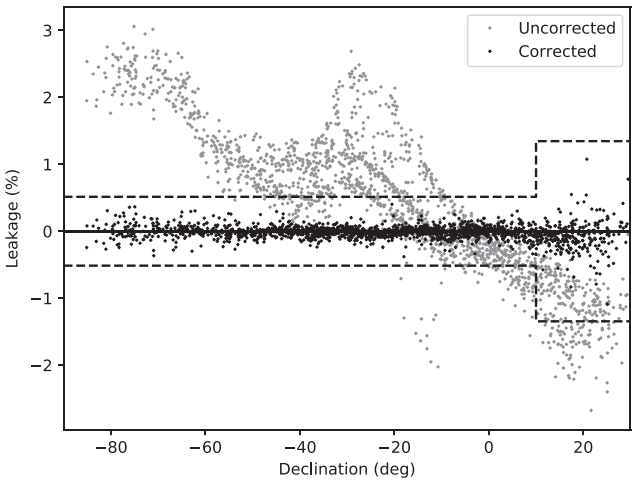

Figure 7. Leakage from Stokes I to Stokes V plotted as a function of declination using GLEAM sources as points of reference in the 200 MHz deep mosaic. Before correction there are clear dependencies with declination whereas after correction the leakage is declination independent. Red dashed lines mark the 6σ region of the scatter in Stokes V leakage after correction, where 1σ = 0.12 per cent for declinations less than +20° and 0.3 per cent for declinations above +20°.

equal proportions having either negative or positive sign. Three pulsars (PSRs J0034−0721, J1136+1551, and J1932+1059) were previously observed with LOFAR at 149 MHz (Noutsos et al. 2015) and exhibit a consistent sign of circular polarization and similar fractional polarization in our 200 MHz observations. Four pulsars (PSRs J0738−4042, J0745−5353, J0835−4510, and J1327−6222) exhibit a sign flip at 200 MHz compared to observations at 1.4 GHz (Johnston & Kerr 2017). PSR J0835−4510 is the most prominent of these given that it is detected with a signal-to-noise ratio of greater than 30. PSR J0745−5353 is detected in circular polarization at 200 MHz but is not detected in Stokes I.

Of the 60 pulsars detected in the GLEAM 200 MHz survey data (Murphy et al. 2017), we detect 11 at the 6σ level – a proportion of ∼18 per cent. We also detect an additional three pulsars that were in regions not explored by GLEAM (e.g. the Galactic plane) or were too faint to be seen in the confusion limited Stokes I maps.

3.2 AGN

It is unusual to find AGN with a fractional circular polarization greater than 0.5 per cent so the three remaining AGNs were examined in more detail. All three AGNs are detected just above our 6σ threshold for residual leakage and the 6σ local noise threshold. Subtle local variations in noise and/or systematic leakage may have been sufficient to push these sources above the threshold. 3C 139.2 itself is situated at the edge of the surveyed region at a declination of ∼+28° where sensitivity is extremely poor. Being situated both at the edge of the field and near the Galactic plane (RA = ∼5.4 h) also limits the effectiveness of leakage subtraction at the source location. Inspection of the 216 MHz mosaic confirms that leakage subtraction was particularly poor at that location and so is likely a false detection.

The two remaining AGNs (PMN J0257−2433 and PKS J0006−4235) have peaks in circular polarization that are significantly offset (>2 arcmin) from the Stokes I peak, offsets that are significantly higher than expected based on the SNR, PSF, and ionosphere. While these may be associated with a chance alignment by a foreground circularly polarized source, it is more likely that these are associated with AGN hot spots. If these hotspots are linearly polarized and exhibit a low RM, they may be symptomatic of leakage from Stokes U to Stokes V. Such leakage results from an uncorrected XY-phase and has been observed to occur with low-RM sources (Lenc et al. 2017) with a fractional leakage of ∼20 per cent. Taylor et al. (2009) determined PMN J0257−2433 was 5 per cent linearly polarized with an RM of 11.7 ± 4.5 rad m^{-2} at 1.4 GHz. If the source exhibits similar characteristics at 200 MHz then Stokes U to Stokes V leakage would be sufficient to cause a false detection in this instance. The same may be true for PKS J0006-4235 as it is morphologically

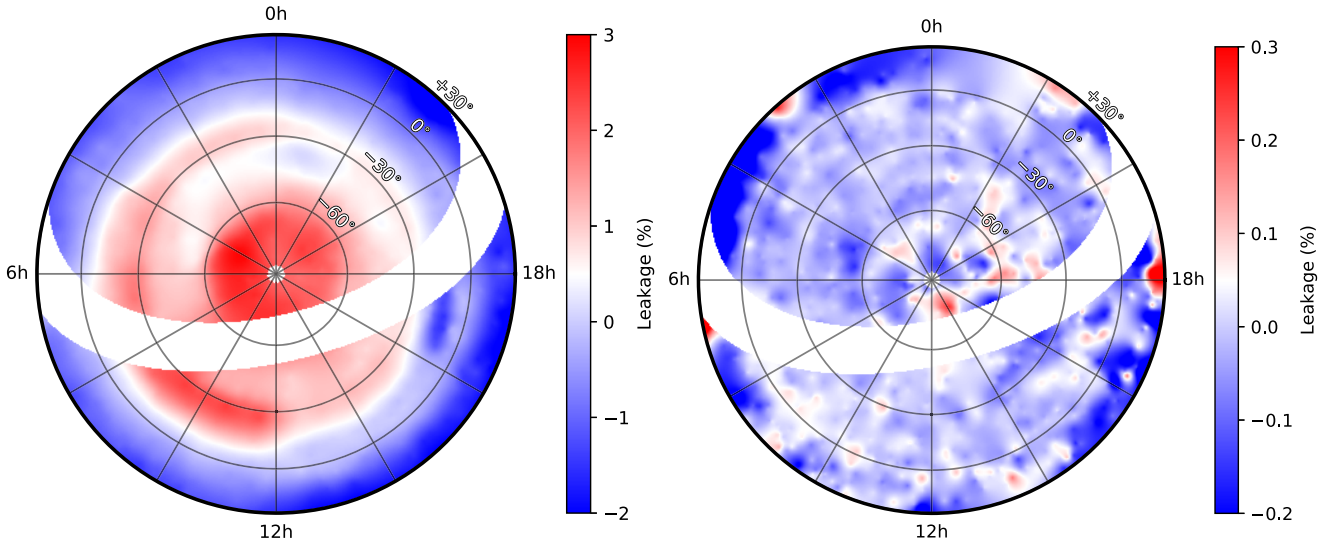

Figure 8. Comparison of measured Stokes I to Stokes V leakage for GLEAM sources in the 200 MHz deep mosaic. The map on the left-hand side shows the leakage before correction and the map on the right after correction. In both maps the blanked strip removes the Galactic plane region as this was not surveyed by GLEAM. Note that the scale in the corrected map is an order of magnitude lower compared to the uncorrected map. ZEA projection is used, centred on a declination of −90°.

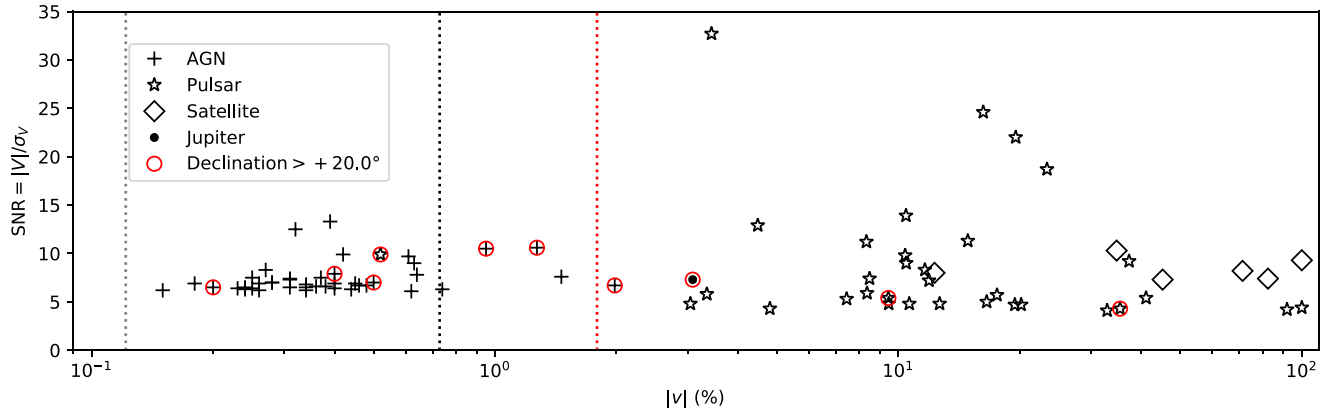

Figure 9. Plot of all blind and targeted detections showing the signal-to-noise of the detection and the absolute percentage circular polarization ($|v|$). The different source types are distinguished by a marker symbol. Sources that are detected above a declination of +20° are circled. The grey dashed line shows the 1σ leakage in Stokes V for declinations below +20°, the black dashed line shows the 6σ leakage in Stokes V for declinations below +20°, and the red dashed line marks the 6σ leakage for declinations above +20°.

similar. The source is known to be a 20 GHz source (Murphy et al. 2010), but its polarimetric characteristics are not known. Further observations of this source would be required to determine its true nature.

3.3 Jupiter

While Jupiter is known to exhibit a fractional circular polarization ∼1 per cent level at 3.24 GHz (Seaquist 1969), we measure ∼3.1 per cent (7.3σ) at 200 MHz. Jupiter was at a relatively high declination (+21.9°) and close to the Galactic plane (7.9 h) in the epoch where it was detected. As with the AGN examined in Section 3.2, the source is in a region where sensitivity is poor and residual leakage is high and this may have resulted in an overestimation or even a false detection. Further observations would be required to confirm this.

3.4 Artificial satellites

Six of the detections in circular polarization at 200 MHz were not associated with any astrophysical sources. Upon closer inspection of the original snapshot images that were integrated to form the all-sky mosaic, it was discovered that each of the detected sources only appeared in a single 2-min snapshot. Further investigation of the original spectral cube for each of the snapshots revealed that the spectral energy distribution for each of the transient sources exhibited narrow-band spikes (see Fig.11) that are commonly associated with radio frequency interference.

It is known that satellites can reflect FM-band signals from the Earth and this can be detected in MWA observations (Tingay et al. 2013b). The result is typically a moving point source that tracks with the location of the satellite as it moves through its orbit. However, the detections found here were in a band that is well above the FM band. Secondly, the detections are unresolved and do not appear

Table 2. List of all sources detected above 6σ at 200 MHz in circular polarization that have an associated astrophysical counterpart. The RA, Dec. are the J2000 position of the peak in MWA 200 MHz mosaic image. The angular separation is the angular distance between source peak and the catalogued position of the nearest identified radio source (see the text for details). V_{200} is the measured Stokes V flux density. SNR is the signal-to-noise ratio of the detected source. S_{200} is the estimated total intensity at 200 MHz. v_{200} is the estimated fractional circular polarization. v_v, and v are the fractional circular polarization and frequency, respectively,found in literature. References provided within parentheses refer to J: Johnston & Kerr (2017), L: this work, M: Murphy et al. (2017), N: Noutsos et al. (2015), X: Xue et al. (2017), and Y: You & Han (2006).

Source	RA (J2000)	Dec (J2000)	Ang. Sep. (arcmin)	V_{200} (mJy)	SNR	S_{200} (ref) (mJy)	v_{200} (per cent)	v_v (per cent)	v (ref) (MHz)
PSR J0034−0721	$00^h34^m10^s$	−07°21′38″	0.3	+30.5	13.9	292.0 (M)	+10.4	+12.0	149 (N)
PSR J0437−4715	$04^h37^m20^s$	−47°14′24″	1.0	+135.4	24.6	834.0 (M)	+16.2	+8.0	438 (Y)
PSR J0630−2834	$06^h30^m51^s$	−28°34′28″	0.5	− 20.7	12.9	463.0 (M)	− 4.5	− 2.8	1400 (J)
PSR J0738−4042	$07^h38^m31^s$	−40°41′56″	0.5	+14.0	7.4	165.0 (M)	+8.5	− 3.7	1400 (J)
PSR J0742−2822	$07^h42^m50^s$	−28°22′29″	0.1	− 15.3	9.0	146.0 (X)	− 10.5	− 2.4	1400 (J)
PSR J0745−5353	$07^h45^m04^s$	−53°52′37″	1.5	− 18.7	9.2			+4.7	1400 (J)
PSR J0835−4510	$08^h35^m22^s$	−45°10′20″	0.6	+243.6	32.7	7075.0 (M)	+3.4	− 6.2	1400 (J)
PSR J1136+1551	$11^h36^m04^s$	+15°50′49″	0.4	− 159.7	18.7	684.0 (M)	− 23.4	− 17.0	149 (N)
PSR J1157−6224	$11^h57^m26^s$	−62°24′06″	1.1	+50.8	11.3	342 (L)	+14.9	+13.2	1400 (J)
PSR J1327−6222	$13^h27^m28^s$	−62°22′00″	1.4	− 33.8	7.2	284.0 (M)	− 11.9	+7.1	1400 (J)
PSR J1453−6413	$14^h53^m40^s$	−64°12′31″	1.0	+57.0	11.2	684.0 (M)	+8.3	+6.9	1400 (J)
PSR J1651−4246	$16^h51^m53^s$	−42°45′56″	0.6	− 213.9	22.0	1095.0 (M)	− 19.5	− 5.6	1400 (J)
PSR J1932+1059	$19^h32^m15^s$	+10°58′47″	0.6	− 58.3	8.3	501.0 (M)	− 11.6	− 22.8	149 (N)
PSR J2048−1616	$20^h48^m35^s$	−16°16′30″	0.2	+17.6	9.8	169.0 (M)	+10.4	+7.1	1400 (J)
PKS J0006−4235[a]	$00^h05^m59^s$	−42°32′19″	2.4	− 12.8	6.3	1718.0 (L)	− 0.74		
PMN J0257−2433[a]	$02^h57^m23^s$	−24°31′37″	2.4	+10.1	7.6	692.4 (L)	+1.5		
3C 139.2[a]	$05^h24^m35^s$	+28°13′27″	1.9	− 227.3	6.7	11486.3 (L)	− 2.0		
Jupiter[a]	$07^h27^m44^s$	+21°54′17″	0.4	− 37.0	7.3	1198.7 (L)	− 3.0		

Note. [a]These sources may be affected by excessive leakage from Stokes I or Stokes U.

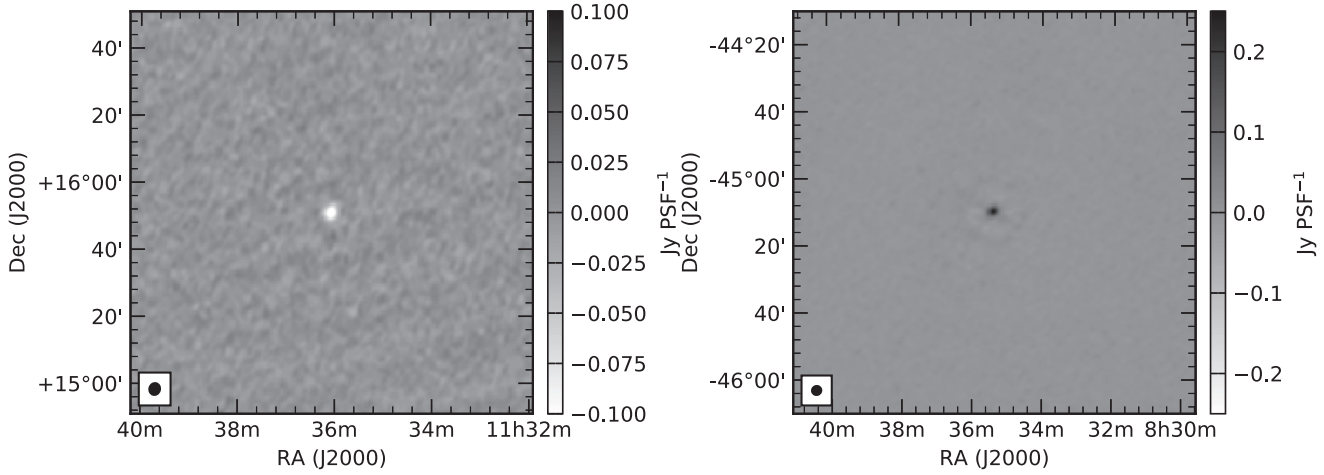

Figure 10. Image of two sample pulsars from 200 MHz deep mosaic showing detections in different signs of circular polarization. Left: PSR J1136+1551 (negative sign). Right: PSR J0835−4510 (positive sign). The synthesized beam is shown inset for PSRs J1136+1551 and J0835−4510, they are 3.5 × 3.2 (position angle −15°) and 2.8 × 2.7 (position angle −68°), respectively.

to move, this suggests that this is as a result of direct short-term transmission from the satellite itself rather than reflection.

To confirm the satellite nature of the detections, satellite ephemeris was obtained from http://space-track.org/. The positions of satellites were tracked over the 2-min period of each snapshot to determine if any corresponded with the position of the detected source. In each instance a satellite was identified within 1 arcmin of the 'transient' source, these are listed in Table 3. The fields were re-imaged at higher time-resolution around the estimated location of a nearby satellite to confirm the association of the flare with the satellite and the time of the flare was also recorded in Table 3.

4 TARGETED SURVEY

4.1 Pulsars

As noted in Section 3.1, the pulsars detected in the blind survey all have relatively high fractional circular polarization. This makes them excellent candidates for a targeted survey. Of the 2613 known pulsars in ATNF Pulsar Catalog (v1.56), 2376 of these are within our survey region. A targeted survey of these pulsars was performed by probing the circular polarization map at each of the pulsar locations (as recorded in the ATNF Pulsar Catalog) for significant emission above the esimated local image noise. For the targeted

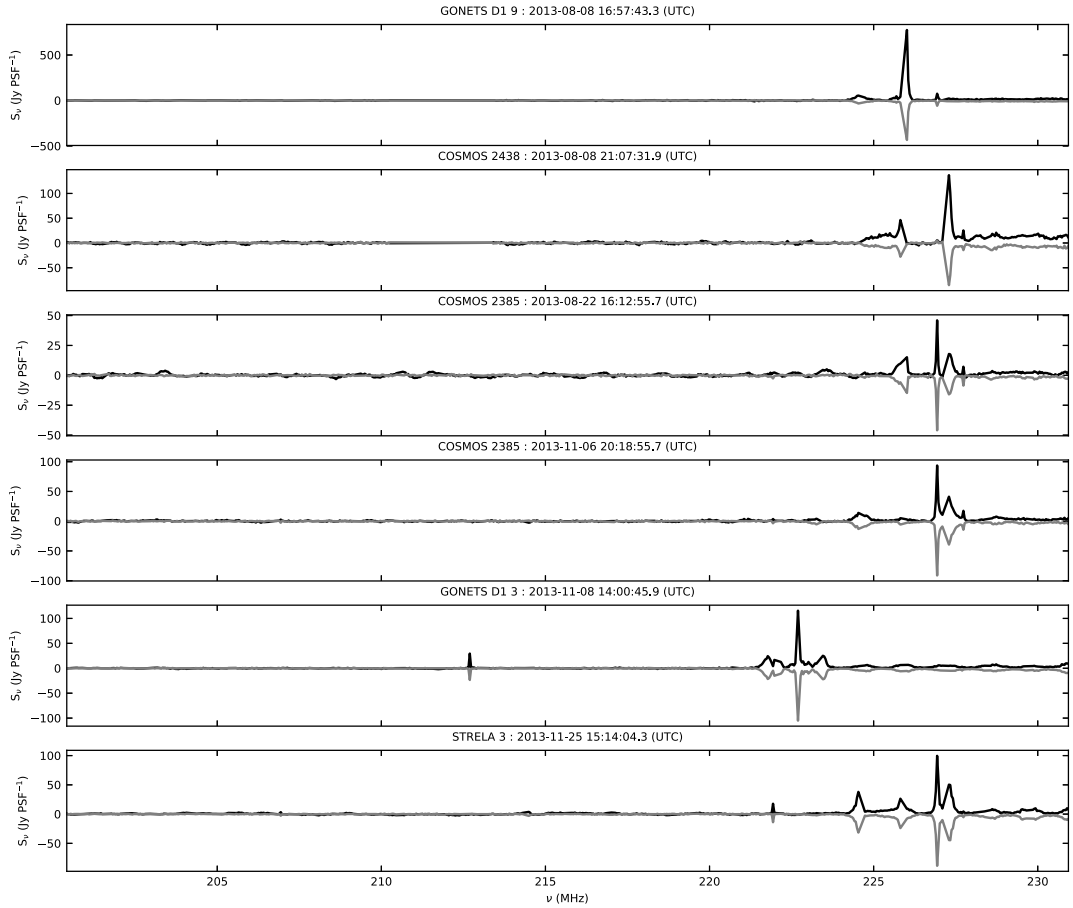

Figure 11. The measured spectral energy distribution of all point-like 'transients' observed in the survey data. Stokes I is shown in black and Stokes V in red. The unusual profile and high degree of circular polarization suggest that these are most likely due to intermittent transmissions from artificial satellites that pass through the observed field.

Table 3. Table of artificial satellite emission detected in circular polarization. The coordinate and time of the satellite are listed at the time of emission. The angular separation is between the observed emission and the predicted location of the satellite based on the satellites ephemeris.

Satellite	NORAD ID	RA (J2000)	Dec (J2000)	Ang. Sep. (arcmin)	Time (UTC)
GONETS D1 9	27060	$21^h59^m06^s$	$+14°02'30''$	0.7	2013-08-08 16:57:43.3
COSMOS 2438	32955	$02^h20^m23^s$	$+10°50'47''$	0.3	2013-08-08 21:07:31.9
COSMOS 2385	27056	$21^h52^m28^s$	$-05°17'59''$	0.6	2013-08-22 16:12:55.7
COSMOS 2385	27056	$07^h47^m45^s$	$-42°28'46''$	0.5	2013-11-06 20:18:55.7
GONETS D1 3	23789	$00^h44^m36^s$	$-51°00'56''$	0.9	2013-11-08 14:00:45.9
STRELA 3	37153	$03^h49^m00^s$	$-31°31'41''$	0.7	2013-11-25 15:14:04.3

survey, a lower (4σ) threshold was utilized compared to the blind survey since an a priori position was known.

Table 4 lists all pulsars that were detected above the 4σ threshold, the table excludes pulsars that were already detected in the blind survey. In total, 32 pulsars were detected, and 18 of these were not detected by the blind survey. All of the pulsars with low-frequency circular polarization previously reported in literature have consistent sign with the detections reported here. Three of the pulsars have a sign flip in circular polarization compared to measurements reported at higher frequencies, i.e. PSRs J0206−4028, J0828−3417, and J1900−2600.

The pulsar catalogue produced by Murphy et al. (2017) for all 60 pulsars detected in total intensity at 200 MHz with the MWA provides an accurate sample against which fractional circular polarization detections and limits can be compared. Murphy et al. (2017) pulsars that were detected in the blind survey and targeted survey have already been listed in Tables 2 and 4, respectively. Table 5 lists all Murphy et al. (2017) pulsars that were not detected above 4σ in circular polarization. When compared against the measured fractional circular polarization in literature, only two of these pulsars, PSRs J0837−4135 and J1752−2806, were expected to be detected at 200 MHz above a 4σ limit. As the previous observations were at 1.4 GHz, it is likely that the polarimetric behviour of these sources is different at 200 MHz. In total, 21 out of 60 Murphy et al. (2017) pulsars are detected above 4σ, a proportion of 35 per cent. Additionally, 11 sources were detected in this survey that were not

Table 4. Targeted pulsars detected above 4σ at 200 MHz in circular polarization. Table columns are the same as defined in Table 2. References provided within parentheses refer to B: Bilous et al. (2016), F: Frail et al. (2016), J: Johnston & Kerr (2017), L: This work, M: Murphy et al. (2017), N: Noutsos et al. (2015), and Y: You & Han (2006).

Pulsar	RA (J2000)	Dec (J2000)	Ang. Sep. (arcmin)	V_{200} (mJy)	SNR	S_{200} (ref) (mJy)	v_{200} (per cent)	v_{ν} (per cent)	ν (ref) (MHz)
J0034−0534	$00^h34^m25^s$	$-05°34'52''$	0.8	− 11.4	5.7	65.0 (M)	− 17.5	− 9.8	149 (N)
J0206−4028	$02^h06^m00^s$	$-40°27'19''$	0.8	− 6.2	4.7	32.0 (M)	− 19.4	+9.3	1400 (J)
J0452−1759	$04^h52^m35^s$	$-17°59'08''$	0.4	+9.1	4.8	96.0 (M)	+9.5	+3.6	1400 (J)
J0820−4114	$08^h20^m14^s$	$-41°14'21''$	0.4	+12.3	4.8	116.0 (M)	+10.6	+4.5	1400 (J)
J0828−3417	$08^h28^m18^s$	$-34°16'22''$	0.8	− 12.2	4.8	400.0 (M)	− 3.0	+5.0	606 (Y)
J1239+2453	$12^h39^m39^s$	$+24°53'34''$	0.4	− 54.8	4.3	154.7 (B)	− 35.4	− 7.5	149 (N)
J1359−6038	$14^h00^m08^s$	$-60°37'23''$	1.5	+29.9	5.3	402.0 (M)	+7.4	+17.3	1400 (J)
J1456−6843	$14^h56^m08^s$	$-68°43'24''$	0.8	+24.8	5.8	738.0 (M)	+3.4	+4.6	1400 (J)
J1543+0929	$15^h43^m40^s$	$+09°28'31''$	0.8	− 29.6	4.8	234.0 (M)	− 12.7	− 33.0	234 (Y)
J1600−5044	$16^h00^m55^s$	$-50°44'06''$	0.4	+23.1	5.0	139.3 (F)	+16.6	+29.3	1400 (J)
J1707−4053	$17^h07^m23^s$	$-40°54'11''$	0.4	− 42.6	5.9	493 (L)	− 8.6	− 3.5	1400 (J)
J1834−0731	$18^h34^m17^s$	$-07°31'52''$	0.8	+30.5	4.2			+14.3	1400 (J)
J1835−0643	$18^h35^m07^s$	$-06°43'21''$	0.4	− 32.8	4.1	99.5 (F)	− 32.9	− 5.3	1400 (J)
J1842−0612	$18^h42^m46^s$	$-06°12'51''$	0.8	+29.1	4.4				
J1900−2600	$19^h00^m46^s$	$-26°00'59''$	0.4	− 14.4	4.3	299.0 (M)	− 4.8	+1.4	1400 (J)
J1921+2153	$19^h21^m46^s$	$+21°52'47''$	0.4	+63.1	5.4	914 (L)	+6.9	+6.8	149 (N)
J2241−5236	$22^h41^m37^s$	$-52°35'51''$	1.1	− 12.1	4.7	60.0 (M)	− 20.1		
J2256−1024	$22^h56^m55^s$	$-10°24'49''$	0.4	+10.0	5.4		+41.1		

detected by Murphy et al. (2017), suggesting that searching for pulsars in circular polarization can help to discover sources that would have been missed in total intensity searches.

We note that the pulsar PSR J2330−2005, previously detected by Lenc et al. (2016) in deep observations at 154 MHz, is not detected in the targeted survey. The source was found to be circularly polarized with a flux density of -8.9 ± 1.1 mJy and -9.6 ± 1.0 mJy in two separate epochs at 154 MHz. In the 200 MHz all-sky survey, our 4σ limit is $|V_{200}| < 7.2$ mJy PSF^{-1} for this source location. When adjusted for the GLEAM spectral index of this source ($\alpha = -0.71 \pm 0.57$), the brightest detection of this source would have an expected circular polarization of -8.0 ± 1.6 at 200 MHz (-7.4 ± 1.6 for the weaker detection). Given the error constraints, it is possible that this source may have fallen below the threshold of this survey. Deeper observations would be required to confirm the nature of this source at 200 MHz.

4.2 Limits on radio emission from exoplanets

The magnetized planets in our Solar system emit intense, low-frequency radio emission associated with planetary aurora. Similarly, planets outside our Solar System (i.e. exoplanets) capable of generating planetary-scale magnetic fields are expected to produce bright radio emission (Winglee et al. 1986; Zarka et al. 2001). The emission is produced via the electron-cyclotron maser instability (CMI), arising from the propagation of energetic electrons along converging magnetic field lines in the magnetosphere of the planet. CMI emission is characterized as bright, beamed, highly circularly polarized radio emission that can be variable on time-scales of seconds to days (Wu & Lee 1979; Treumann 2006). Because the emitting frequency of the planetary radio emission is tied magnetic field strength, radio detections of exoplanets will directly measure their field strengths and in turn provide insight into the interior composition of these planets. Additionally, the variations of the radio emission in time and frequency variability can provide geometrical constraints on the planet's orbit and magnetic field configuration (Hess & Zarka 2011).

There have been many observational attempts to detect radio emission from exoplanets (Bastian, Dulk & Leblanc 2000; Lazio et al. 2004; George & Stevens 2007; Lazio & Farrell 2007; Smith et al. 2009; Lazio et al. 2010; Stroe, Snellen & Röttgering 2012; Hallinan et al. 2013; Lecavelier des Etangs et al. 2013; Sirothia et al. 2014; Murphy et al. 2015; Lynch et al. 2017a; O'Gorman et al. 2018), but there have been no unambiguous detections to date. The expected high fractional circular polarization of CMI emission makes exoplanets prime targets for Stokes V searches. Two previous studies have used Stokes V imaging with the MWA to search for radio emission from exoplanets. From a catalogue of 1 110 known exoplanets (as of 2014 May 14), Murphy et al. (2015) targeted 17 sources that they identified as having estimated flux densities and emission frequencies close to or above the MWA detection capabilities. Lynch et al. (2017a) observed a young star-forming region to search for variable Stokes V emission that might be associated with exoplanets in still forming planetary systems.

Since the publication of Murphy et al. (2015), many thousands of exoplanets have been discovered through various optical techniques (Schneider et al. 2011). Using an updated catalogue of 4132 sources (known population of exoplanets as of 2018 February 19), we did a targeted search of the 1 506 sources located within our survey region for significant circularly polarized emission above the estimated local image noise. Again, we used a lower, 4σ threshold since an a priori position was known. Of the 1 506 sources searched, two sources, Proxima Cen b and HD 34445 b, were found to be associated with emission at a $>4\sigma$ level.

Visually inspecting the Stokes V image for HD 34445 b, we found the source has structure in the image that was indicative of a noise peak in the image; thus, we ruled this source out as a detection. Visual inspection of the Proxima Centauri b image found the emission to be point-like and an investigation of the associated Stokes I emission did not reveal a bright source that could be responsible for any total intensity leakage. We tentatively claim to make a detection of weak emission at the location of Proxima Centauri b, however the detected radio emission is not expected to be associated with the planet but instead with the host star.

Table 5. Non-detections from Murphy et al. (2017) catalogue of 200 MHz pulsars. Upper limits are specified at 4σ at 200 MHz in circular polarization. S_{200} is the total intensity at 200 MHz taken from Murphy et al. (2017). $|v_{200}|$ is the upper limit of the fractional circular polarization at 200 MHz. Table columns are the same as defined in Table 2. References provided within parentheses refer to B: Bilous et al. (2016), F: Frail et al. (2016), J: Johnston & Kerr (2017), L: This work, M: Murphy et al. (2017), N: Noutsos et al. (2015), and Y: You & Han (2006).

Pulsar	$\lvert V_{200}\rvert$ (mJy)	S_{200} (mJy)	$\lvert v_{200}\rvert$ (per cent)	v_v (per cent)	v (ref) (MHz)
J0737−3039A	<4.3	53.0	<8.1		
J0809−4753	<11.8	229.0	<5.2	−0.4	1400 (J)
J0820−1350	<7.4	160.0	<4.6	−4.2	1400 (J)
J0826+2637	<31.8	243.0	<13.1	+6.2	149 (N)
J0837+0610	<12.4	286.0	<4.3	−2.6	149 (N)
J0837−4135	<11.8	95.0	<12.5	+13.8	1400 (J)
J0840−5332	<12.0	56.0	<21.4	+9.0	660 (Y)
J0855−3331	<9.7	47.0	<20.6		
J0856−6137	<12.1	85.0	<14.3	+5.6	1400 (J)
J0905−5127	<13.6	73.0	<18.6	+14.1	1400 (J)
J0907−5157	<12.2	106.0	<11.6	+4.8	1400 (J)
J0922+0638	<15.2	100.0	<15.2	+5.6	1400 (J)
J0924−5302	<10.9	96.0	<11.3	−7.3	1400 (J)
J0942−5552	<11.4	73.0	<15.7	+0.6	1400 (J)
J0942−5657	<14.1	112.0	<12.6	+11.6	1400 (J)
J0953+0755	<13.6	1072.0	<1.3	−11.5	149 (N)
J0959−4809	<13.6	50.0	<27.1	−4.0	1400 (J)
J1001−5507	<14.3	142.0	<10.0	+1.9	1400 (J)
J1012−2337	<8.2	47.0	<17.4		
J1047−3032	<7.6	24.0	<31.8		
J1057−5226	<16.2	202.0	<8.0	+3.2	1400 (J)
J1116−4122	<9.2	52.0	<17.6	−3.6	1400 (J)
J1121−5444	<17.8	101.0	<17.6	−7.8	1400 (J)
J1430−6623	<15.8	190.0	<8.3	+4.5	1400 (J)
J1543−0620	<12.9	91.0	<14.1	−5.0	234 (Y)
J1607−0032	<71.8	137.0	<52.4	+1.4	1400 (J)
J1643−1224	<21.4	123.0	<17.4	−1.0	1331 (Y)
J1645−0317	<23.0	774.0	<3.0	−0.1	1400 (J)
J1651−1709	<20.2	111.0	<18.2		
J1722−3207	<16.7	229.0	<7.3	+3.9	1400 (J)
J1731−4744	<24.6	325.0	<7.6	+5.4	1400 (J)
J1752−2806	<22.8	1504.0	<1.5	+5.9	1400 (J)
J1810+1744	<110.0	231.0	<47.6		
J1820−0427	<28.9	499.0	<5.8	−3.3	1400 (J)
J1824−1945	<24.3	177.0	<13.7	+1.3	1400 (J)
J1824−2452A	<20.0	199.0	<10.1		
J1913−0440	<20.6	176.0	<11.7	−7.0	149 (N)
J2053−7200	<15.4	110.0	<14.0	−4.0	660 (Y)
J2155−3118	<7.6	46.0	<16.5	−13.8	1400 (J)

CMI emission is emitted at the cyclotron frequency of the source population of the electrons, which is directly related to the local magnetic field strength, B_p, of the planetary magnetosphere:

$$f_c = \frac{eB_p}{2\pi m_e} \approx 2.8 \text{ MHz } B_p \quad (1)$$

where m_e and e are the electron mass and charge, respectively, and B_p is measured in Gauss. The maximum estimated magnetic field strength for Proxima Centauri b is 1 Gauss (Burkhart & Loeb 2017), corresponding to a maximum emission frequency of ∼3 MHz. Due to ionospheric absorption of emission at frequencies <10 MHz, planetary radio emission from Proxima Centauri b cannot be detected by ground-based radio telescopes. Thus any emission that we detected using ground-based radio telescopes must be related to the magnetic activity of the star; the possibility of Proxima Centauri producing the observed emission is discussed in the next section.

The upper limits set by this survey for a set of best radio detection candidate exoplanets, as identified by their theoretically estimated emission frequencies and radio flux densities, will be discussed in a future paper (Lynch et al. 2018).

4.3 Limits on radio emission from flare stars

Some magnetically active stars are observed to exhibit short-duration, narrow-band, and highly circularly polarized (∼100 per cent) radio flares. The observed polarization and frequency-time structure of these flares points to a coherent emission mechanism such as CMI (Bastian et al. 2000; Güdel 2002). In the 1960s–1970s several magnetically active M dwarf stars were observed at frequencies between 90 and 300MHz using single-dish telescopes. These observations revealed bright radio flares with rates between 0.03 and 0.8 flares per hour and intensities ranging from 0.8 to 20 Jy. However, recent low-frequency surveys to detect transients have resulted in non-detections (e.g. Rowlinson et al. 2016; Tingay et al. 2016).

To confirm the previous M dwarf stellar flare rates and flux densities at 100–200 MHz, Lynch et al. (2017b) targeted UV Ceti, a magnetically active M dwarf star. As the radio flares from UV Ceti were expected to be highly circularly polarized, this search was focused in the circularly polarized images rather than in total intensity. Four flares were detected from UV Ceti with flux densities a factor of 100 fainter than those in the literature.

Following this example, we used the updated catalogue of radio stars by Wendker (2015) to search for circularly polarized emission associated with the positions of these objects. A wide variety of stellar objects are included in this catalogue including M dwarf stars, RS CVn binaries, and magnetic chemically peculiar hot stars. This catalogue contains 3021 objects, 2400 of which are located within our survey region. From this search we identify three objects associated with emission at a >4σ level: Proxima Centauri, HR 5942, and DM-64 1685. Visual inspection of the circularly polarized image for D-64 1685 ruled it out as a detection, as the emission structure more closely resembles that of image noise than point-source like. In the total intensity image, the location of HR 5942 offset from a bright extragalactic source leaving us to conclude that the observed Stokes V emission is not due to total intensity leakage. A similar offset is found for both Stokes Q and U and not indicative of linear polarization leakage. We tentatively claim a 4.5σ detection of HR 5942 with a measured Stokes V flux density of -11 ± 3 mJy. Additionally, we claim a tentative detection of Proxima Centauri, with a measured flux density of -18 ± 4 mJy.

Both HR 5942 and Proxima Centauri are previously detected in the radio. HR 5942 is a magnetic chemically peculiar Bp star with previous detections of quiescent emission at 5 and 14 GHz (Linsky, Drake & Bastian 1992; Leone, Trigilio & Umana 1994) and radio flaring at 5 GHz (Drake & Linsky 1989); both types of emission are thought to be gyrosynchrotron emission. Coherent emission has been observed in other magnetic chemically peculiar stars from 610 to 1400 MHz (Trigilio et al. 2000; Chandra et al. 2015; Das, Chandra & Wade 2018). If the detection of HR 5942 is confirmed, this would be the lowest frequency detection of a magnetic chemically peculiar hot star and only the third hot star to be observed emitting highly circularly polarized, coherent emision. Proxima Centauri is an emission-line M dwarf star, previously observed to emit bright coherent bursts at ∼1 GHz (Lim, White & Slee 1996; Slee, Willes & Robinson 2003). Other M dwarf stars have been ob-

served to emit radio emission from MHz to GHz frequencies (e.g. AD Leo: Spangler, Rankin & Shawhan 1974; Jackson, Kundu & White 1989; YZ CMi: Spangler & Moffett 1976; Kundu & Shevgaonkar 1988). Given the previously observed GHz bursts from Proxima Centauri, it is possible that this source could also produce bursts at 170–230 MHz; a previous 3σ limit of 42.3 mJy at 200 MHz has been reported by Bell et al. (2016). To further confirm the tentative detections of HR 5942 and Proxima Centauri, investigation into the variability and frequency spectrum of the observed emission is ongoing.

5 CONCLUSIONS

We have demonstrated the effectiveness of polarization leakage mitigation using MWA observations and have used it to complete an all-sky survey in circular polarization using existing observations. The fractional leakage was typically reduced by an order of magnitude to less than 0.72 per cent and allowed both blind and targeted surveys to be performed with a sensitivity of 1.0–3.0 mJy PSF^{-1}.

We have detected 32 pulsars, 6 transient emissions from artificial satellites, and 2 flare stars. When compared against total intensity observations of pulsars at 200 MHz, 35 per cent of pulsars that were detectable in total intensity were also detected in circular polarization. Furthermore, 11 pulsars detected in circular polarization were not originally found in total intensity (as a result of their location in the Galactic plane or the limited sensitivity available in Stokes I because of confusion). The two flare stars detected in this survey were only detected in circular polarization due to either limited sensitivity in the total intensity image or the close proximity of a nearby, bright extragalactic source. Of the 3610 exoplanets in our catalogue of known objects, 1506 exoplanets were located within our survey region; these were also searched but did not yield any detections.

The all-sky survey presented here was not ideal for detecting transient emission from sources such as flare stars and exoplanets. Transient sources and sources that can change sign in polarization, such as seen with the flare star UV Ceti (Lynch et al. 2017b), require an alternate observing and processing strategy. To avoid diluting the signal, the integration of the snapshot images should not exceed the time-scale of the expected emission before a sign flip occurs or the emission stops. Similarly, for periodic emission where the duty cycle is low, tracked observations of a field would be better suited to increase the probability of catching the moment of the flaring emission. Two avenues of investigation that will be pursued in future will be to search through overlapping snapshot images of the drift-scan for transient emission and to apply the leakage mitigation techniques developed here to targeted observations.

While an order-of-magnitude improvement in Stokes I to Stokes V leakage has been greatly beneficial, further improvements would be required to probe sources with low levels of fractional circular polarization. The technique presented in this paper is currently limited by sidelobe confusion, noise, and fitting of the 2D model of the position-dependent leakage. A more extended antenna array, such as that available with the recent MWA extension, can help reduce PSF sidelobes and improve the sensitivity of uniform-like imaging. Sensitivity can also be improved by avoiding beam-former or frequency changes over the course of a drift-scan. With a near-continuous drift-scan, field sources can probe leakage over much finer tracks throughout the field. Finally, improved 2D modelling can also help to reduce errors at the field edges where increased residual leakage is noticed. Currently a simply 2D quadratic function is used for fitting: more complex functions may improve the fitting results.

An outstanding challenge not addressed in the survey presented here is distinguishing between Stokes U to Stokes V leakage and true circular polarization. This is only problematic for sources with both a significant degree of linear polarization and with a low RM. As such, it only affects a small sub-set of candidate sources. To determine the effect of this leakage requires knowledge of the X-Y phase that is typically obtained by observing a linearly polarized source. Such sources are rare at long wavelengths, however, it may be possible to measure the effect in diffuse linearly polarized Galactic emission (Lenc et al. 2017). The practicality and effectiveness of this are yet to be investigated for an all-sky survey.

The methods for leakage mitigation demonstrated here should also be applicable to Square Kilometre Array Low Frequency array (SKA-LOW).[2] The method requires minimal processing and is fast because no deconvolution is required. The main requirement is that the nature of the leakage remains constant for instrumental beam. A secondary requirement is that good-quality images can be generated on relatively small time-scales. In the case of the MWA, the large number of available baselines enables it to generate good-quality images on 2-min time-scales. The current specification for SKA-low has fewer baselines compared to the MWA but they will be more sensitive and more extended. As long as this compromise does not adversely affect the quality of the snapshot dirty maps, the mitigation techniques used for the MWA should still be effective with SKA-Low.

ACKNOWLEDGEMENTS

The authors thank Ron Ekers for useful discussions. TM acknowledges the support of the Australian Research Council through grant FT150100099. DLK was supported by NSF grant AST-1412421. This scientific work makes use of the Murchison Radio-astronomy Observatory, operated by CSIRO. We acknowledge the Wajarri Yamatji people as the traditional owners of the Observatory site. Support for the operation of the MWA is provided by the Australian Government (NCRIS), under a contract to Curtin University administered by Astronomy Australia Limited. We acknowledge the Pawsey Supercomputing Centre, which is supported by the Western Australian and Australian Governments. This research was conducted by the Australian Research Council Centre of Excellence for All-sky Astrophysics (CAASTRO), through project number CE110001020. This research has made use of the NASA/IPAC Extragalactic Database, which is operated by the Jet Propulsion Laboratory, California Institute of Technology, under contract with the National Aeronautics and Space Administration. The authors thank the anonymous referee for providing useful comments on the original version of this paper.

REFERENCES

Aller H. D., Aller M. F., 2012, Am. Astron. Soc., 220, 335.20
Bastian T. S., Dulk G. A., Leblanc Y., 2000, ApJ, 545, 1058
Bell M. E. et al., 2016, Astron. Telegram, 9465
Bernardi G. et al., 2013, ApJ, 771, 105

[2]See SKA phase 1 system (Level 1) requirements SKA-TEL-SKO-0000008: http://www.skatelescope.org/wp-content/uploads/2014/03/SKA-TEL-SKO-0000008-AG-REQ-SRS-Rev06-SKA1_Level_1_System_Requirement_Specification-P1-signed.pdf

Bertin E., Mellier Y., Radovich M., Missonnier G., Didelon P., Morin B., 2002, in Bohlender D. A., Durand D., Handley T. H., eds, ASP Conf. Ser. Vol. 281, Astronomical Data Analysis Software and Systems XI, Astron. Soc. Pac., San Francisco, p. 228
Bhat N. D. R., Cordes J. M., Camilo F., Nice D. J., Lorimer D. R., 2004, ApJ, 605, 759
Bilous A. V. et al., 2016, A&A, 591, A134
Burkhart B., Loeb A., 2017, ApJ, 849, L10
Cenacchi E., Kraus A., Beckert T., Mack K., 2011, in Bastien P., Manset N., Clemens D. P., St-Louis N., eds, ASP Conf. Ser. Vol. 449, Astronomical Polarimetry 2008: Science from Small to Large Telescopes, Astron. Soc. Pac., San Francisco, p. 426
Chandra P. et al., 2015, MNRAS, 452, 1245
Condon J. J., Cotton W. D., Greisen E. W., Yin Q. F., Perley R. A., Taylor G. B., Broderick J. J., 1998, AJ, 115, 1693
Das B., Chandra P., Wade G. A., 2018, MNRAS, 474, L61
Drake S. A., Linsky J. L., 1989, in Haisch B. M., Rodonò M., eds, Solar and Stellar Flares. Poster Papers, Vol. 104, Catania Astrophysical Observatory, Catania, Italy, . p. 41
Enßlin T. A., Hutschenreuter S., Vacca V., Oppermann N., 2017, Phys. Rev. D, 96, 043021
Frail D. A. et al., 2018, MNRAS, 475, 942
Frail D. A., Jagannathan P., Mooley K. P., Intema H. T., 2016, ApJ, 829, 119
George S. J., Stevens I. R., 2007, MNRAS, 382, 455
Geyer M. et al., 2017, MNRAS, 470, 2659
Güdel M., 2002, ARA&A, 40, 217
Hallinan G., Sirothia S. K., Antonova A., Ishwara-Chandra C. H., Bourke S., Doyle J. G., Hartman J., Golden A., 2013, ApJ, 762, 34
Hess S. L. G., Zarka P., 2011, A&A, 531, A29
Hurley-Walker N. et al., 2014, PASA, 31, e045
Hurley-Walker N. et al., 2017, MNRAS, 464, 1146
Hurley-Walker N., 2017, preprint (arXiv:1703.06635)
Intema H. T., Jagannathan P., Mooley K. P., Frail D. A., 2017, A&A, 598, A78
Jackson P. D., Kundu M. R., White S. M., 1989, A&A, 210, 284
Johnston S., Kerr M., 2017, MNRAS, 474, 4629
Komesaroff M. M., Roberts J. A., Milne D. K., Rayner P. T., Cooke D. J., 1984, MNRAS, 208, 409
Kundu M. R., Shevgaonkar R. K., 1988, ApJ, 334, 1001
Lazio T. J. W., Farrell W. M., 2007, ApJ, 668, 1182
Lazio W. T. J., Farrell W. M., Dietrick J., Greenlees E., Hogan E., Jones C., Hennig L. A., 2004, ApJ, 612, 511
Lazio T. J. W., Shankland P. D., Farrell W. M., Blank D. L., 2010, AJ, 140, 1929
Lecavelier des Etangs A., Sirothia S. K., Gopal-Krishna Zarka P., 2013, A&A, 552, A65
Lenc E. et al., 2016, ApJ, 830, 38
Lenc E. et al., 2017, PASA, 34, e040
Leone F., Trigilio C., Umana G., 1994, A&A, 283, 908
Lim J., White S. M., Slee O. B., 1996, ApJ, 460, 976
Linsky J. L., Drake S. A., Bastian T. S., 1992, ApJ, 393, 341
Loi S. T. et al., 2015, Geophys. Res. Lett., 42, 3707
Lynch C. R., Murphy T., Kaplan D. L., Ireland M., Bell M. E., 2017a, MNRAS, 467, 3447
Lynch C. R., Lenc E., Kaplan D. L., Murphy T., Anderson G. E., 2017b, ApJ, 836, L30
Lynch C. R., Murphy T., Lenc E., Kaplan D. L., 2018, MNRAS, in press
Macquart J. P., Kedziora-Chudczer L., Rayner D. P., Jauncey D. L., 2000, ApJ, 538, 623
Macquart J.-P., 2002, Publ. Astron. Soc. Aust., 19, 43
Macquart J.-P., 2003, New Astron. Rev., 47, 609
Manchester R. N., Hobbs G. B., Teoh A., Hobbs M., 2005, AJ, 129, 1993
Mauch T., Murphy T., Buttery H. J., Curran J., Hunstead R. W., Piestrzynski B., Robertson J. G., Sadler E. M., 2003, MNRAS, 342, 1117
Mitchell D. A., Greenhill L. J., Wayth R. B., Sault R. J., Lonsdale C. J., Cappallo R. J., Morales M. F., Ord S. M., 2008, IEEE J. Select. Topi. Signal Proc., 2, 707
Murphy T. et al., 2010, MNRAS, 402, 2403
Murphy T. et al., 2015, MNRAS, 446, 2560
Murphy T. et al., 2017, PASA, 34, e020
Noutsos A. et al., 2015, A&A, 576, A62
O'Gorman E., Coughlan C. P., Vlemmings W., Varenius E., Sirothia S., Ray T. P., Olofsson H., 2018, A&A, 612, A52
O'Sullivan S. P., McClure-Griffiths N. M., Feain I. J., Gaensler B. M., Sault R. J., 2013, MNRAS, 435, 311
O'Sullivan S. P., Lenc E., Anderson C. S., Gaensler B. M., Murphy T., 2018, MNRAS, 475, 4263
Offringa A. R., van de Gronde J. J., Roerdink J. B. T. M., 2012, A&A, 539, A95
Ord S. M. et al., 2010, PASP, 122, 1353
Rayner D. P., Norris R. P., Sault R. J., 2000, MNRAS, 319, 484
Rengelink R. B., Tang Y., de Bruyn A. G., Miley G. K., Bremer M. N., Roettgering H. J. A., Bremer M. A. R., 1997, A&AS, 124, 259
Riseley C. J., Lenc E., Van Eck C. L., Heald G., Gaensler B. M., Anderson C. S., Hancock P. J., Sridhar S. S., 2018, PASA, submitted
Rowlinson A. et al., 2016, MNRAS, 458, 3506
Schneider J., Dedieu C., Le Sidaner P., Savalle R., Zolotukhin I., 2011, A&A, 532, A79
Seaquist E. R., 1969, Nature, 224, 1011
Sirothia S. K., Lecavelier des Etangs A., Gopal-Krishna Kantharia N. G., Ishwar-Chandra C. H., 2014, A&A, 562, A108
Slee O. B., Willes A. J., Robinson R. D., 2003, PASA, 20, 257
Smith A. M. S., Collier Cameron A., Greaves J., Jardine M., Langston G., Backer D., 2009, MNRAS, 395, 335
Sokolowski M., , et al., 2017, PASA, 34, e062, ,
Spangler S. R., Moffett T. J., 1976, ApJ, 203, 497
Spangler S. R., Rankin J. M., Shawhan S. D., 1974, ApJ, 194, L43
Stroe A., Snellen I. A. G., Röttgering H. J. A., 2012, A&A, 546, A116
Sutinjo A., O'Sullivan J., Lenc E., Wayth R. B., Padhi S., Hall P., Tingay S. J., 2015, Radio Sci., 50, 52
Taylor A. R., Stil J. M., Sunstrum C., 2009, ApJ, 702, 1230
Tingay S. J. et al., 2013a, PASA, 30, e007
Tingay S. J. et al., 2013b, AJ, 146, 103
Tingay S. J., Hancock P. J., Wayth R. B., Intema H., Jagannathan P., Mooley K., 2016, AJ, 152, 82
Treumann R. A., 2006, A&A Rev., 13, 229
Trigilio C., Leto P., Leone F., Umana G., Buemi C., 2000, A&A, 362, 281
van Straten W., Manchester R. N., Johnston S., Reynolds J. E., 2010, PASA, 27, 104
Wayth R. B. et al., 2015, PASA, 32, e025
Weiler K. W., de Pater I., 1983, ApJS (ISSN 0067-0049), 52, 293
Wendker H. J., 2015, VizieR Online Data Catalog, 8099
Winglee R. M., Dulk G. A., Bastian T. S., 1986, ApJ, 309, L59
Wu C. S., Lee L. C., 1979, ApJ, 230, 621
Xue M. et al., 2017, PASA, 34, e070
You X.-P., Han J.-L., 2006, Chin. J. Astron. Astrophys. Suppl., 6, 56
Zarka P., Treumann R. A., Ryabov B. P., Ryabov V. B., 2001, Ap&SS, 277, 293

This paper has been typeset from a TEX/LATEX file prepared by the author.